Nilesh D. Pawar
Department of Mechanical Engineering,
Indian Institute of Technology Delhi,
Hauz Khas, New Delhi 110016, India

Sunil R. Kale
Department of Mechanical Engineering,
Indian Institute of Technology Delhi,
Hauz Khas, New Delhi 110016, India

Supreet Singh Bahga
Department of Mechanical Engineering,
Indian Institute of Technology Delhi,
Hauz Khas, New Delhi 110016, India

Hassan Farhat
Department of Mechanical Engineering,
Wayne State University,
Detroit, MI 48202

Sasidhar Kondaraju[1]
School of Mechanical Sciences,
Indian Institute of Technology Bhubaneswar,
Argul, Odisha 752050, India
e-mail: sasidhar@iitbbs.ac.in

Study of Microdroplet Growth on Homogeneous and Patterned Surfaces Using Lattice Boltzmann Modeling

We present droplet growth dynamics on homogeneous and patterned surfaces (surface with hydrophilic and hydrophobic region) using two-dimensional thermal lattice Boltzmann method (LBM). In the first part, we performed 2D simulations on homogeneous hydrophobic surfaces. The result shows that the droplet grows at higher rate on a surface with higher wettability which is attributed to low conduction resistance and high solid–liquid contact area. In the later part, we performed simulations on patterned surface and observed that droplet preferentially nucleates on the hydrophilic region due to lower energy barrier and grows in constant contact line (CCL) mode because of contact line pinning at the interface of hydrophilic–hydrophobic region. As the contact angle reaches the maximum value of hydrophobic surface, contact line depins and droplet shows constant contact angle (CCA) growth mode. We also discuss the effect of characteristic width of hydrophilic region on growth of droplet. We show that contact angle of the droplet increases rapidly and reaches the contact angle of hydrophobic region on a surface with a lower width of the hydrophilic surface. [DOI: 10.1115/1.4043175]

1 Introduction

Condensation heat transfer has a wide range of applications in power generation [1], water harvesting [2], water desalination [3], cooling of a nuclear reactor [4], and thermal management of electronic devices [5]. Enhancement of condensation heat transfer has the capability to substantially improve thermal efficiency and, hence, cost of energy consumption in these applications.

Depending on the wettability of the condensing surface, condensation is categorized as either filmwise condensation (FWC) or dropwise condensation (DWC). In FWC, the condensate forms a liquid film on the surface. This liquid film act as an additional thermal resistance to heat transfer between the surface and the vapor. Whereas, in DWC, the vapor condenses in the form of distinct liquid drops. The DWC provides an order of magnitude higher heat transfer rate compared to FWC because of recurrent cycles of droplet nucleation, growth, coalescence, and departure from the surface [6].

Previous studies have shown that it is difficult to sustain DWC for a long period. Sustenance of DWC depends on the efficient removal of condensed droplets from the surface for which it is essential to understand how these drops grow on different wettability surfaces. Graham and Griffith [7] studied the effect of droplet size on heat transfer during DWC and showed that the droplet smaller than of $\mathcal{O}(10 \ \mu m)$ in diameter contributed more than 50% of the overall heat transfer, although the surface coverage of such drops was less than 10%. Leach et al. [8] also showed that the rate of condensation per unit area is high for small droplets of $\mathcal{O}$ (10–20 μm). Later, Rykaczewski [9] reported two distinct growth modes namely, constant contact line (CCL) and constant contact angle (CCA) growth mode.

Droplets preferentially nucleate on the hydrophilic surface due to lower energy barrier to form the nucleus. However, high contact angle hysteresis makes it difficult for the removal of a droplet from the surface. Whereas, the hydrophobic surface has low contact angle hysteresis and the droplet can be removed easily. To take advantage of both preferential nucleation of droplets on the hydrophilic surface and their ease of movement on the hydrophobic surface, patterned surfaces (surface with hydrophilic and hydrophobic regions) can be used. Varanasi et al. [10] reported that spatial control of nucleation sites could be achieved by controlling intrinsic wettability of the surface. Hou et al. [11] showed that liquid condensation forms a film on the superhydrophilic region and transforms into a droplet shape as it reaches the interface of superhydrophilic and superhydrophobic regions. Despite extensive studies, individual droplet growth dynamics is not well understood since spatial and temporal resolutions limit experiments from obtaining all the information regarding droplet growth.

Condensation heat transfer has been widely analyzed experimentally in past decades. However, the numerical studies on dropwise condensation are limited due to complex processes involved, such as droplet nucleation, growth, coalescence, and departure from the surface. A few numerical studies on condensation have been reported by solving Navier–Strokes equations in the liquid and vapor phases, respectively [12–14]. The conservation equations for each phase are coupled through boundary conditions at the interface [15]. An interface is tracked by the level set function in level set method and the volume fraction in the volume of fluid approach. However, it is difficult to handle an interface which rapidly evolves with time. Besides, it significantly increases the computational cost.

In past two decades, lattice Boltzmann method (LBM) has developed into an efficient and powerful simulation tool for multiphase flows [16–18] and phase change heat transfer [19] compared to Navier–Strokes simulations. Shan and Chen [20,21] proposed pseudo-potential lattice Boltzmann model to simulate multiphase flows. They introduced pseudo-potential ψ to simulate nonlocal interactions between the particles. The model naturally captures the dynamic nature of the interface due to interparticle interaction forces. To further improve the Shan and Chen model in terms of density ratio, spurious currents, and temperature range, Yuan and Schaefer [22] incorporated different equations of state,

---

such as, van der Waals, Peng-Robinson, etc. But the multiphase Shan and Chen model is limited to isothermal flows only. To solve the macroscopic energy equation, another distribution function is commonly used. This additional distribution function of temperature is then coupled with flow field at the macroscopic level via an equation of state. Gong and Cheng [23] presented a pseudopotential thermal LBM to simulate the liquid–vapor phase change heat transfer. They used two distribution functions, one for flow field and the other for temperature field. They devised a source term to model phase change heat transfer and added to the temperature distribution function. The model was later used by Liu and Cheng [24] to simulate two-dimensional filmwise condensation on a vertical flat plate. The same authors implemented the model for simulation of dropwise condensation on a vertical flat plate [25]. They studied droplet formation, growth, and departure from the surface. Ashrafi and Moosavi [26] performed two-dimensional simulations to investigate droplet nucleation and growth on homogeneous hydrophilic surfaces ($45\,\mathrm{deg} < \theta \le 90\,\mathrm{deg}$). However, to the best of our knowledge, we know of no numerical study focusing on microdroplet growth on homogeneous hydrophobic ($90\,\mathrm{deg} < \theta < 150\,\mathrm{deg}$) and patterned surfaces.

In this paper, we present the microdroplet growth on homogeneous hydrophobic and patterned surfaces using thermal lattice Boltzmann method. The model takes into account the two-phase hydrodynamics, wetting at the solid surface, and phase change heat transfer. In particular, we show the effect of surface wettability on droplet growth for hydrophobic surfaces. We also show the droplet growth mechanism on patterned surfaces, and moreover, the effect of characteristic width of the hydrophilic region on droplet growth dynamics. We begin by reviewing the thermal lattice Boltzmann model. We then present model validation cases and the simulation results.

2 Numerical Modeling

In the framework of the LBM, we take into account two-phase hydrodynamics, wetting dynamics at the solid surface, and liquid–vapor phase change heat transfer. We outline the lattice Boltzmann modeling here. The model presented here is mostly same as the Gong and Cheng model. In the derivation of energy equation, Gong and Cheng assumed the term ρc_v as a constant. However, the term ρc_v varies significantly within the liquid–vapor interface. To take into account variation of the term ρc_v, in this study, we used the energy source term given by Li et al. [27].

2.1 Lattice Boltzmann Model.
The evolution equation of the particle distribution function with Bhatnagar–Gross–Krook (BGK) collision operator is given as [28]

$$f_i(\mathbf{x} + \mathbf{e}_i\delta t, t + \delta t) - f_i(\mathbf{x}, t) = \frac{-1}{\tau}\left[f_i(\mathbf{x}, t) - f_i^{\mathrm{eq}}(\mathbf{x}, t)\right] + \triangle f_i(\mathbf{x}, t) \tag{1}$$

where $f_i(\mathbf{x}, t)$ is the particle distribution function in the ith direction with discrete particle velocity $\mathbf{e}_i$ at location $\mathbf{x}$ and time t, τ is the non-dimensional relaxation time, and $f_i^{\mathrm{eq}}(\mathbf{x}, t)$ is the corresponding equilibrium distribution function which is given as [29]

$$f_i^{\mathrm{eq}}(\mathbf{x}, t) = \rho w_i\left[1 + \frac{(\mathbf{e}_i \cdot \mathbf{u})}{c_s^2} + \frac{(\mathbf{e}_i \cdot \mathbf{u})^2}{2c_s^4} - \frac{\mathbf{u}^2}{2c_s^2}\right] \tag{2}$$

where $c_s = c/\sqrt{3}$ is the lattice speed of sound, $c = \delta x/\delta t$ is the lattice speed, δx is the lattice spacing, and δt is the lattice time-step. For two-dimensional simulations, we used D2Q9 lattice arrangement which has nine discrete velocities.

The weighting coefficients ω_i and the discrete particle velocities $\mathbf{e}_i$ for D2Q9 model are given by

$$w_i = \begin{cases} 4/9, & i = 0 \\ 1/9, & i = 1, 2, 3, 4 \\ 1/36, & i = 5, 6, 7, 8 \end{cases}$$

$$\mathbf{e}_i = \begin{cases} (0, 0), & i = 0 \\ (\pm 1, 0)c, (0, \pm 1)c, & i = 1, 2, 3, 4 \\ (\pm 1, \pm 1)c, & i = 5, 6, 7, 8 \end{cases}$$

The lattice Boltzmann equation (1) is solved in two steps: collision and streaming.

(1) *Collision*: The particles arriving at a node collide and change their direction. The post collision distribution functions are calculated as

$$f_i^*(\mathbf{x}, t) = f_i(\mathbf{x}, t) - \frac{1}{\tau}\left[f_i(\mathbf{x}, t) - f_i^{\mathrm{eq}}(\mathbf{x}, t)\right] \tag{3}$$

(2) *Streaming*: The particles move to the neighboring node corresponding to their velocity directions

$$f_i(\mathbf{x} + \mathbf{e}_i\delta t, t + \delta t) = f_i^*(\mathbf{x}, t) \tag{4}$$

To implement the body force term $\triangle f_i(\mathbf{x}, t)$, we used the exact difference method (EDM) proposed by Kupershtokh [30]

$$\triangle f_i(\mathbf{x}, t) = f_i^{\mathrm{eq}}(\rho(\mathbf{x}, t), \mathbf{u} + \triangle \mathbf{u}) - f_i^{\mathrm{eq}}(\rho(\mathbf{x}, t), \mathbf{u}) \tag{5}$$

where $\triangle \mathbf{u} = \mathbf{F}\delta t/\rho$ is velocity change due to the action of total force $\mathbf{F}$ during the time-step δt. The macroscopic density ρ and velocity $\mathbf{u}$ are calculated from the distribution function by

$$\rho = \sum_i f_i = \sum_i f_i^{\mathrm{eq}} \tag{6}$$

$$\rho \mathbf{u} = \sum_i f_i \cdot \mathbf{e}_i + \frac{\delta t}{2}\mathbf{F} = \sum_i f_i^{\mathrm{eq}} \cdot \mathbf{e}_i + \frac{\delta t}{2}\mathbf{F} \tag{7}$$

The kinematic viscosity υ is calculated using the relaxation time τ by

$$\upsilon = c_s^2\left(\tau - \frac{1}{2}\right)\delta t \tag{8}$$

2.2 The Pseudo-Potential Multiphase Lattice Boltzmann Model.
For single-component multiphase flow, the interaction force acting on the particles at site $\mathbf{x}$ is given by [20,21]

$$\mathbf{F}_{\mathrm{int}}(\mathbf{x}) = -G\psi(\mathbf{x})\sum_i w_i\psi(\mathbf{x} + \mathbf{e}_i\delta t)\mathbf{e}_i \tag{9}$$

where G is a parameter that controls the strength of the interaction force. The pseudo-potential $\psi(\mathbf{x})$ is taken as [22]

$$\psi(\mathbf{x}) = \sqrt{\frac{2\left(p - \rho c_s^2\right)}{Gc_s^2}} \tag{10}$$

where p represents the pressure. During the calculation of interaction force term using Eq. (9), G gets canceled out. The need of G is to ensure that the entire term inside the square root in Eq. (10) is positive. Therefore, we used $G = -1$ in this study. The p in Eq. (10) is calculated using Peng–Robinson (P–R) equation of state [22] as given by

$$p = \frac{\rho RT}{1 - b\rho} - \frac{a\rho^2\varepsilon(T)}{1 + 2b\rho - b^2\rho^2} \tag{11}$$

$$\varepsilon(T) = \left[1 + (0.37464 + 1.54226\omega - 0.26992\omega^2)\left(1 - \sqrt{\frac{T}{T_{cr}}}\right)\right]^2$$

where a, b denotes the constant parameters, and R is the gas constant. Since the critical point is a point of inflection and it satisfies the following two conditions: $(\partial p/\partial \rho)_{T_{cr}} = 0$ and $(\partial^2 p/\partial \rho^2)_{T_{cr}} = 0$. Using equation of state Eq. (11) along with these conditions gives $a = 0.4572R^2 T_{cr}^2/p_{cr}$ and $b = 0.0778RT/p_{cr}$. Following Refs [22] and [31], we set $a = 2/49$, $b = 2/21$, and $R = 1$ in our simulations. To simulate wettability of the surface, it is essential to incorporate the interaction force between the fluid and the solid wall. Sukope and Thorne [32] proposed following interaction force

$$\mathbf{F}_{ads}(\mathbf{x}) = -G_{ads}\psi(\mathbf{x})\sum_i w_i s(\mathbf{x} + \mathbf{e}_i\delta t)\mathbf{e}_i \tag{12}$$

The parameter G_{ads} controls the strength of the interaction force between the fluid and the solid wall. The different contact angles are obtained by adjusting G_{ads} values and $s(\mathbf{x} + \mathbf{e}_i\delta t)$ is an indicator function which is expressed as

$$s(\mathbf{x} + \mathbf{e}_i\delta t) = \begin{cases} 0 & \text{if } (\mathbf{x} + \mathbf{e}_i\delta t) \text{ is fluid node} \\ 1 & \text{if } (\mathbf{x} + \mathbf{e}_i\delta t) \text{ is solid node} \end{cases}$$

Since, the droplet radius R is much smaller than the capillary length scale which is given as $l = \sqrt{\sigma/\rho g}$ (≈ 2.7 mm for water), we have neglected the effect of gravity. Therefore, the total force acting at each site $\mathbf{x}$ is given by

$$F(\mathbf{x}) = F_{int}(\mathbf{x}) + F_{ads}(\mathbf{x}) \tag{13}$$

2.3 The Phase Change Thermal Lattice Boltzmann Model for Energy Equation. Modeling condensation involves solving the following energy equation [27]:

$$\frac{\partial T}{\partial t} + \nabla \cdot (\mathbf{u}T) = \frac{1}{\rho c_v}\nabla \cdot (\lambda\nabla T) + T\left[1 - \frac{1}{\rho c_v}\left(\frac{\partial p}{\partial T}\right)_\rho\right]\nabla \cdot \mathbf{u} \tag{14}$$

where T is the macroscopic temperature, α is the thermal diffusivity and c_v is the specific heat at constant volume. To solve equation Eq. (14), we used the distribution function for temperature given by [23]

$$g_i(\mathbf{x} + \mathbf{e}_i\delta t, t + \delta t) - g_i(\mathbf{x}, t) = \frac{-1}{\tau_g}\left[g_i(\mathbf{x}, t) - g_i^{eq}(\mathbf{x}, t)\right] + \delta t\, w_i\phi \tag{15}$$

where $g_i(\mathbf{x}, t)$ is the temperature distribution function along the ith direction, τ_g is the dimensionless relaxation time for temperature, ϕ is the source term to model vapor–liquid phase change heat transfer, and $g_i^{eq}(\mathbf{x}, t)$ is its corresponding equilibrium temperature distribution which is given as

$$g_i^{eq}(\mathbf{x}, t) = Tw_i\left[1 + \frac{\mathbf{e}_i \cdot \mathbf{u}}{c_s^2} + \frac{(\mathbf{e}_i \cdot \mathbf{u})^2}{2c_s^4} - \frac{\mathbf{u}^2}{2c_s^2}\right] \tag{16}$$

The macroscopic temperature T is calculated from the temperature distribution function by

$$T = \sum_i g_i \tag{17}$$

The thermal diffusivity α is calculated using the relaxation time of temperature τ_g by

$$\alpha = c_s^2\left(\tau_g - \frac{1}{2}\right)\delta t \tag{18}$$

The source term for liquid–vapor phase change process is given as [27]

$$\phi = T\left[1 - \frac{1}{\rho c_v}\left(\frac{\partial p}{\partial T}\right)_\rho\right]\nabla \cdot \mathbf{u} + \left[\frac{1}{\rho c_v}\nabla \cdot (\lambda\nabla T) - \nabla \cdot \left(\frac{\lambda}{\rho c_v}\nabla T\right)\right] \tag{19}$$

Different viscosity ratios can be achieved by expressing relaxation time as a linear function of local fluid density [31,33]

$$\tau(\rho) = \frac{(\tau_l - \tau_v)}{(\rho_l - \rho_v)}\rho + \frac{(\tau_v\rho_l - \tau_l\rho_v)}{(\rho_l - \rho_v)} \tag{20}$$

where τ_l and τ_v are the relaxation times corresponding to coexistence densities of liquid and vapor phases. Different thermal diffusivity ratios can be obtained similarly.

3 Code Validation

To validate our model, we have performed two test cases which are phase transition at constant temperature and wettability test.

3.1 Phase Transition Process. We simulated two-dimensional phase transition process at a constant temperature. The computational domain was taken as 200×200 lattice units with periodic boundary condition in all directions. The simulation was initialized by giving $\rho = 0.9\rho_{cr} + \triangle\rho$, where $\triangle\rho$ is the small random perturbation. The segregation of liquid and vapor phases occurs due to the interaction forces. The corresponding liquid and vapor densities were quantified from the simulation results. This process was repeated over a range of temperatures. The densities of the liquid and the vapor phases calculated from the simulation were compared with theoretical Maxwell construction as shown in Fig. 1. The simulated results compare well with theoretical Maxwell construction.
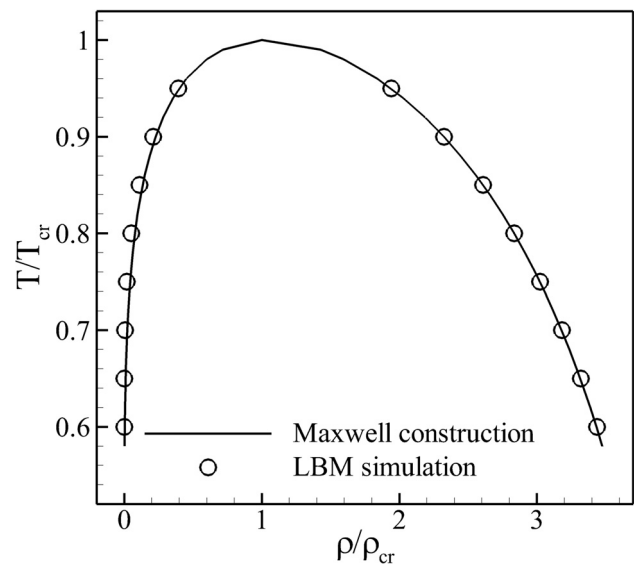

Fig. 1 Comparison of the liquid and vapor density variation with temperature between Maxwell construction and results obtained from our simulations
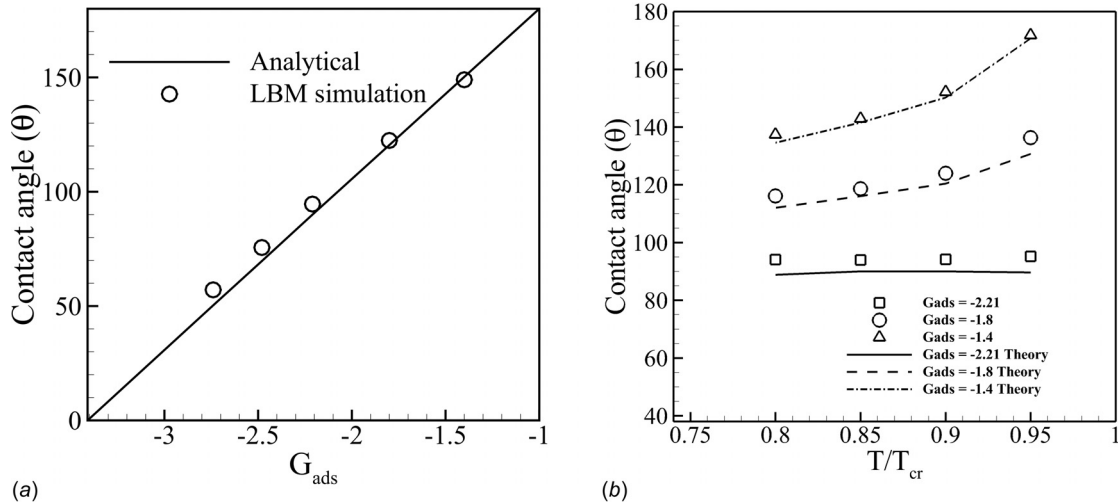
Fig. 2 (*a*) The equilibrium static contact angle θ as a function of solid–fluid interaction parameter G_{ads}. The contact angle increases linearly with G_{ads}. (*b*) Effect of temperature on the static contact angle of the surface for a fixed G_{ads} value.

3.2 Wettability Test. We used a computational domain of 200×200 lattice units with the bounce-back condition in the *y*-direction and the periodic boundary condition in the *x*-direction. A droplet of radius 25 lattice unit was placed at the center of the bottom wall. The different static contact angles were obtained by adjusting G_{ads} values as shown in Fig. 2(*a*). The results obtained are in agreement with the theoretical predictions by Sukope and Throne [32]. In Fig. 2(*b*), we present the effect of temperature on the static contact angle of the surface θ for a fixed G_{ads} value. For all the G_{ads} values considered here, our simulation results agree with the theoretical predictions [32]. We found that for $G_{ads} = -2.21$, the static contact angle is same for all the temperatures. However, for other G_{ads} values, the static contact angle decreases with temperature.

4 Results and Discussion

4.1 Droplet Growth on Homogeneous Surface. A schematic of the computational domain is shown in Fig. 3(*a*). Two-dimensional simulations were carried out in a square domain of $Lx \times Ly$ lattice units. Two walls were defined at the bottom and the top of the domain. Periodic boundary condition was specified in the *x*-direction. For the walls, mass conserving bounce-back scheme given by Briant et al. [34] and the constant temperature condition [35] were employed. The temperature of the saturated vapor was initially fixed at $T_s = 0.9 T_{cr}$ [25]. The corresponding coexistence properties of the liquid and vapor are listed in Table 1. The unit conversion between physical and lattice units for all physical quantities is provided in Supplementary Information document S1 available in the Supplemental Materials on the

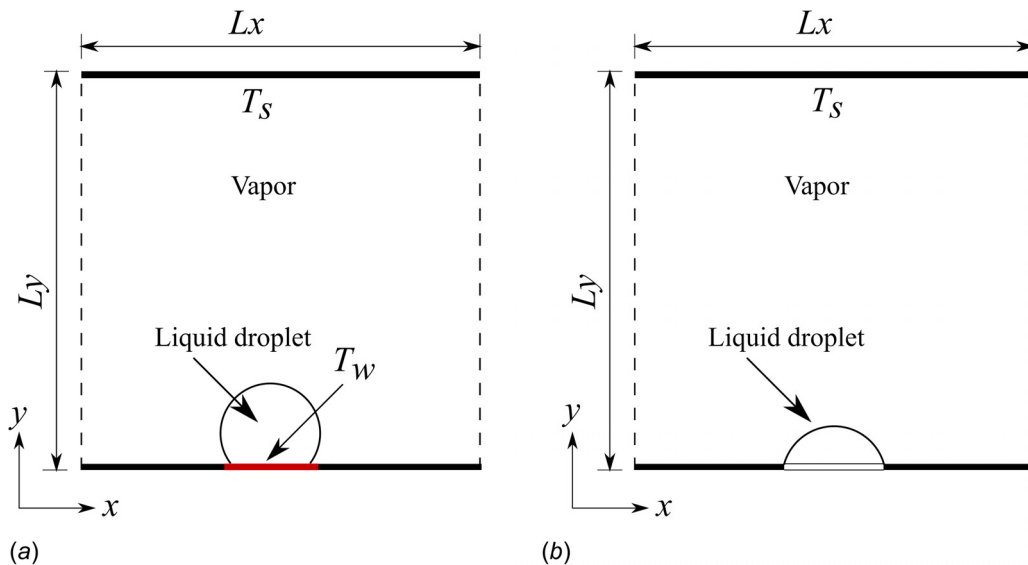Fig. 3 Schematic of the computational domain. The mass conserving bounce-back condition was specified at *y* = 0 and *y* = *Ly*, and periodic condition in *x*-direction. The temperature of the saturated vapor was initially fixed at $T_s = 0.9 T_{cr}$. (*a*) For Homogeneous surface, at the bottom wall, we created a cold spot (shown in red color) by lowering the wall temperature to $T_w = 0.75 T_{cr}$. The top wall temperature was fixed at T_s. (*b*) Patterned surface with hydrophilic and hydrophobic regions. The white and black sections denote hydrophilic and hydrophobic regions, respectively. The bottom wall was maintained at a lower temperature of $T_w = 0.854 T_{cr}$, while the temperature of the top wall was maintained at T_s.

Table 1   Simulation parameters used in this work in both physical and lattice units at T_s = 582.39 K

Parameters	Liquid		Vapor	
	Physical units	Lattice units	Physical units	Lattice units
Density (ρ)	692.37 kg /m^3	5.9081	53.85 kg /m^3	0.5801
Kinematic viscosity (ν)	1.19×10^{-7} m^2 /s	0.1060	3.74×10^{-7} m^2 /s	0.3333
Thermal diffusivity (α)	1.26×10^{-7} m^2 /s	0.1126	2.01×10^{-7} m^2 /s	0.1785
Specific heat (c_v)	3.0447 kJ /kg K	6.6960	3.084 kJ /kg K	6.6960
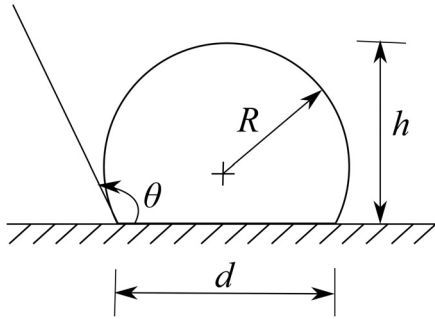
Fig. 4   A schematic of the liquid droplet represented as a cylindrical cap of radius of curvature *R*, base diameter *d*, height *h*, and contact angle θ with the solid surface

Table 2   Droplet radius *R* for three different grid sizes measured at time *t* = 3.3 ms

Grid size	Droplet radius R (μm)
500×500	9.3161
1000×1000	10.1247
1500×1500	10.3714

ASME Digital Collection. At the bottom wall, we created a cold spot of 40 lattice units by fixing the wall temperature to $T_w = 0.75 T_{cr}$. The rest of the wall was at T_s. The cold spot acts as a nucleation site. As the drop grows, we extend the cold spot size to the size of droplet base diameter to ensure that the temperature underneath the drop is $T_w = 0.75 T_{cr}$.

The position of the liquid–vapor interface was identified where the fluid density is given by $\rho_{interface} = (\rho_l + \rho_v)/2$. The shape of the condensed droplet was assumed to be a cylindrical cap of a radius R, base diameter d, height h, and contact angle θ with the solid surface as shown in Fig. 4. The radius R of the droplet is calculated as

$$R = \frac{d^2}{8h} + \frac{h}{2} \tag{21}$$

The contact angle of the droplet is given as

$$\sin \theta = \frac{d}{2R} \tag{22}$$

The volume of the cylindrical droplet V is given as

$$V = R^2 (\theta - \sin \theta \cos \theta) \tag{23}$$

We performed the grid-independent study to check the effect of grid size on the simulation results. We performed simulations for three different grid resolutions namely, 500×500, 1000×1000, and 1500×1500 lattice units while keeping the same length of the computational domain and the thermophysical properties of the fluid. We quantified the droplet radius for three different grid resolutions which are listed in Table 2 at time $t = 3.3$ ms. We found that the difference of droplet radius between 1000×1000 and 1500×1500 grid sizes was 2.4%. Therefore, for all simulations reported in this work, we used grid size of 1000×1000 lattice units.

In a controlled environment, the growth of a condensing droplet is described by the well-known power law $R \sim t^{\mu}$, where μ is the power law exponent. From experimental and theoretical studies, it is reported that $\mu = 1/3$ for three-dimensional droplet growing on

a solid surface [36–38]. In this work, we have performed two-dimensional simulations to investigate droplet growth. By simple scaling analysis illustrated by Beysens [38], we obtained the growth power law for the two-dimensional droplet. The volume (area for 2D droplet) of a droplet is proportional to the droplet radius R as

$$V \sim R^2 \tag{24}$$

Since the droplet volume grows with time, volume is also proportional to time as

$$V \sim t \tag{25}$$

From Eqs. (24) and (25), we get $R \sim t^{\mu}$, where $\mu = 1/2$. Ashrafi and Moosavi [26] also demonstrated the same power law exponent from the condensation growth model.

To analyze the effect of surface wettability on the growth dynamics of a single droplet, we varied the static contact angle of the surface θ. Figures 5(a) and 5(b) shows the time evolution of droplet profile during condensation on a homogeneous surface with the contact angle of 115 deg and 140 deg, respectively. Movies of their evolution are given in the Supplementary Material as S2 and S3, respectively, available in the Supplemental Materials on the ASME Digital Collection. The inset plots of Fig. 5 shows the variation of the dynamic contact angle with time. The change in contact angle is not more than 7% in both cases, which for all practical purposes can be considered as CCA mode. The effect of surface wettability can be studied with regard to the evolution of droplet radius R with time as shown in Fig. 6. Our simulation shows that growth of droplet radius is in good agreement with theoretical growth power law of $R \sim t^{1/2}$.

The rate of heat transfer through the droplet to the surface can be estimated from the volumetric condensation rate of the droplet. Figure 7 shows the condensation rate as a function of time for the three surfaces. The data smoothing was done to reduce the fluctuations associated with the calculation of condensation rate from discrete data points. Irrespective of surfaces, condensation rate first increases and then decreases with time. This behavior is because the droplet initially has a high surface to volume ratio due to its small size resulting in low conduction resistance. However, as the droplet grows the surface to volume ratio decreases drastically leading to high conduction resistance. This implies that small size droplets offer higher condensation performance compared to large droplets. We find that the lower the static contact angle θ of the surface, higher is the condensation rate on the surface. The faster condensation rate on a surface with lower contact
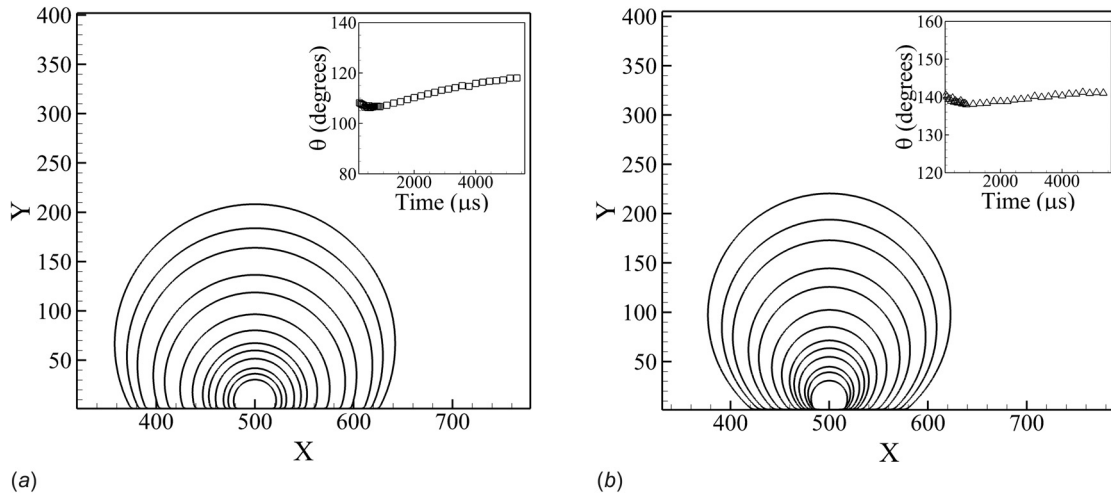
Fig. 5 Time evolution of droplet profile during condensation on a homogeneous surface at different instants of time. The inset plot shows the variation of dynamic contact angle with time: (*a*) $\theta = 115$ deg and (*b*) $\theta = 140$ deg. Movies of their evolution are given in the Supplementary Materials S2 and S3 available in the Supplemental Materials on the ASME Digital Collection.
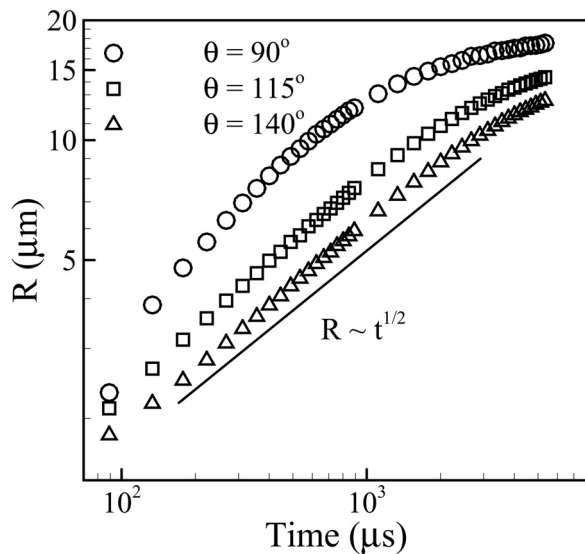

Fig. 6 Temporal evolution of droplet radius for different wettability surfaces. The droplet radius increases with time and follows the growth power law $R \sim t^{\mu}$. The exponent μ is found to be 1/2.

Fig. 7 Effect of surface wettability on condensation rate as a function of time for the three surfaces

angle is attributed to lower conduction resistance and the higher solid–liquid contact area of the droplet.

We also investigated the effect of wall subcooling on droplet growth dynamics. The degree of subcooling is defined as the difference between the saturation temperature of vapor and that of condensing surface and is expressed as $\triangle T = T_s - T_w$. In our simulations, the saturation temperature was fixed at $T_s = 0.9 T_{cr}$ and bottom wall temperature T_w has changed correspondingly. Figure 8 shows the evolution of droplet radius with time for a surface with a static contact angle of 115 deg with three different wall subcooling. We observed that droplet grows at a faster rate as the wall subcooling increases.

4.2 Droplet Growth on Patterned Surface. A schematic of the computational domain for the patterned surface is shown in Fig. 3(*b*). The boundary conditions are same as in Sec. 4.1. Unless
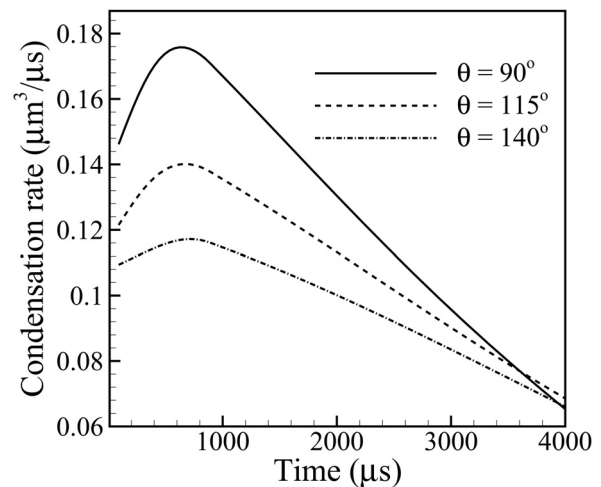
it is specified, all the results are reported for the patterned surface with a width of the hydrophilic region $w = 4\ \mu m$. The temperature of the saturated vapor was initially fixed at $T_s = 0.9 T_{cr}$. The bottom wall was maintained at a lower temperature of $T_w = 0.854 T_{cr}$, while the temperature of the top wall was maintained at T_s.

According to classical nucleation theory, the energy barrier ΔG for droplet nucleation depends on the static contact angle of the surface θ [39]

$$\Delta G = \pi \sigma_{lv} r^{*2}(2 - 3\cos\theta + \cos^3\theta)/3 \qquad (26)$$

where σ_{lv} is the surface tension of the liquid–vapor interface, θ is the static contact angle, and r^* is the critical droplet radius and is given as $(2T_s \sigma_{lv})/(h_{f_g} \rho_l \Delta T)$. The energy barrier ΔG is lowest for $\theta = 0$ deg and maximum for $\theta = 180$ deg. Therefore, droplet preferentially nucleates on the surface with lower contact angle. The nucleation rate is related to the energy barrier ΔG as

$$J = J_0 \exp\left(-\frac{\Delta G}{kT}\right) \qquad (27)$$
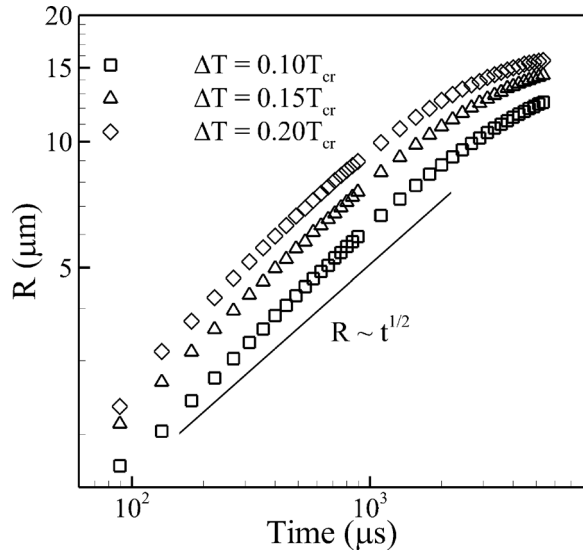
Fig. 8 Effect of wall subcooling on growth dynamics of a droplet. The droplet grows at a faster rate as the wall subcooling increases.

Table 3 Test cases for patterned surfaces with 4 μm hydrophilic region

	Contact angle θ	
Patterned surface	Hydrophilic region (deg)	Hydrophobic region (deg)
A	10	140
B	10	115

where J_0 is a kinetic constant, k is the Boltzmann constant, and T is the surface temperature. The nucleation time t is inversely proportional to the nucleation rate J [39]

$$t \propto \frac{1}{J} \tag{28}$$
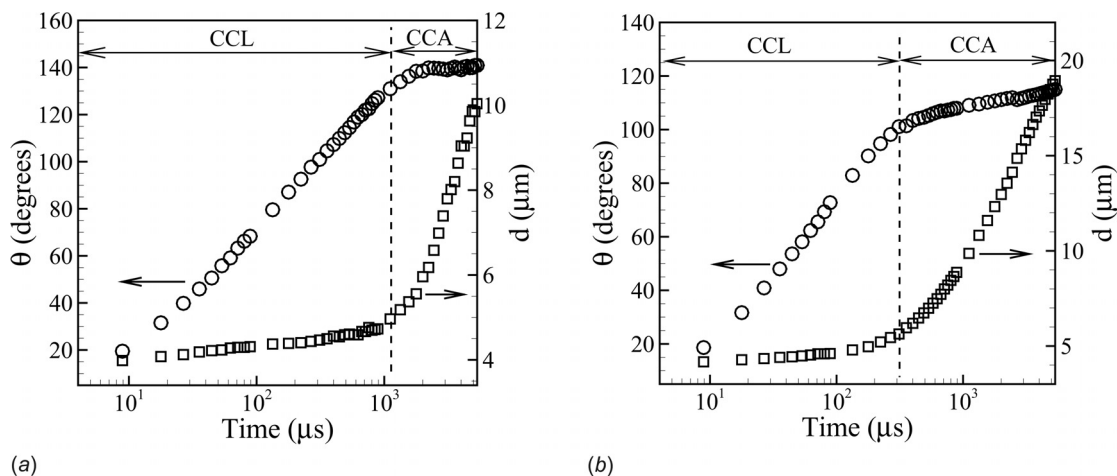
Therefore, $t_{hydrophobic} \gg t_{hydrophilic}$. Hence, only single droplet forms on the hydrophilic region of the patterned surface for the time period for which simulations were performed.

To understand the growth dynamics of a droplet on the patterned surfaces, the following test cases listed in Table 3 were performed. Figure 9(a) shows the temporal evolution of droplet base diameter d and contact angle θ for the patterned surface A (video of the droplet growth on surface A is provided in the Supplementary Martetial as S4 available in the Supplemental Materials on the ASME Digital Collection). We found that for the patterned surface, the droplet preferentially nucleates on the hydrophilic region and spreads rapidly in the lateral direction forming a wet spot. Due to the effect of contact line pinning at the interface of the hydrophilic–hydrophobic region, the condensate droplet is found to grow in CCL growth mode and, as a result, the contact angle increases over the time. In CCL growth mode, the contact angle of the droplet increases and reaches the maximum value of 140 deg. After that, the contact line depins and droplet growth shows CCA growth mode while the contact line moves forward into the hydrophobic region. The results are consistent with the experiments of Hou et al. [11] and Rykaczewski [9], and the molecular dynamics simulations performed by Xu et al. [40].

The droplet growth on surface B exhibits the same behavior as on surface A (shown in Fig. 9(b)). However, we observed that contact line pinning effect is strong on surface A. This behavior is expected because the droplet needs more time to reach the contact angle of hydrophobic region which is 140 deg.

Figure 10 shows the streamline pattern inside and outside of the droplet in CCL ($t = 0.03$ ms) and CCA ($t = 5.34$ ms) mode. The droplet shape is shown by a red line. In CCL mode, condensation occurs both at the contact line as well as at the liquid–vapor interface of the droplet. It is evident by the flow of vapor at the liquid–vapor interface and the contact line of the droplet. However, in CCA mode vapor primarily condenses at the contact line of the droplet. This disparity in both the modes is because of the different contact angles of the droplet that determines the total thermal resistance of the condensation heat transfer. In CCA mode, the contact angle is higher than that of CCL mode, resulting in higher thermal resistance. Consequently, droplet grows at a faster rate in CCL mode.

We also analyzed the effect of characteristic width of the hydrophilic region w on growth dynamics of the droplet. We have performed simulations on three different types of patterned surfaces with the width of hydrophilic region $w = 4 \mu$m, $w = 8 \mu$m, and

(a)

(b)

Fig. 9 Temporal evolution of droplet base diameter d and contact angle θ for the patterned surface. Droplet preferentially nucleates on the hydrophilic region, rapidly spreads laterally forming a wet spot on the hydrophilic region which leads to CCL mode. In CCL mode, contact angle increases and reach the maximum value corresponding to hydrophobic region. After that contact line depins and droplet shows CCA mode while the contact line moves forward into the hydrophobic region: (a) surface A and (b) surface B.
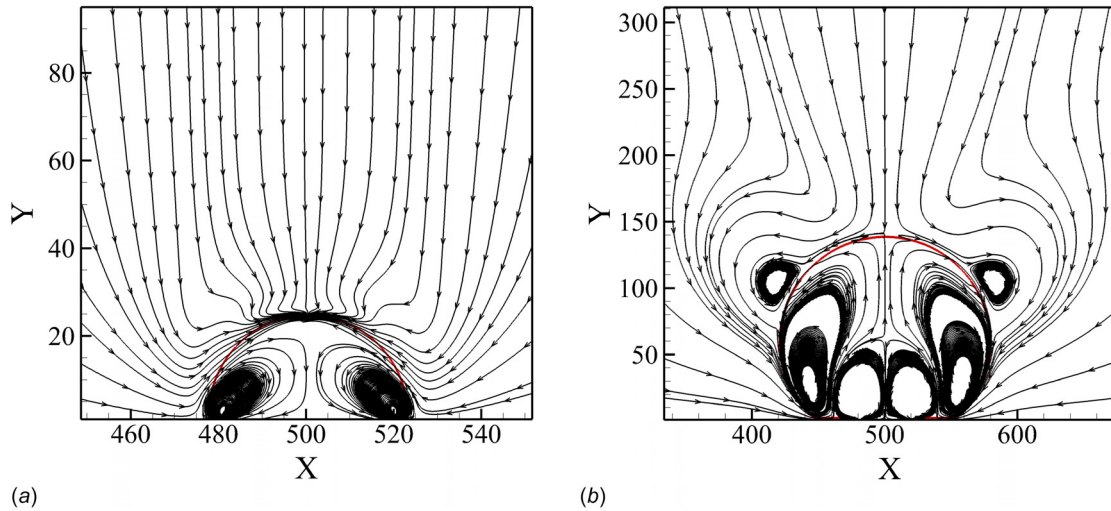
Fig. 10 Streamline pattern inside and outside of the droplet. The droplet shape is shown by a red line: (*a*) CCL mode (*t* = 0.03 ms) and (*b*) CCA mode (*t* = 5.34 ms).
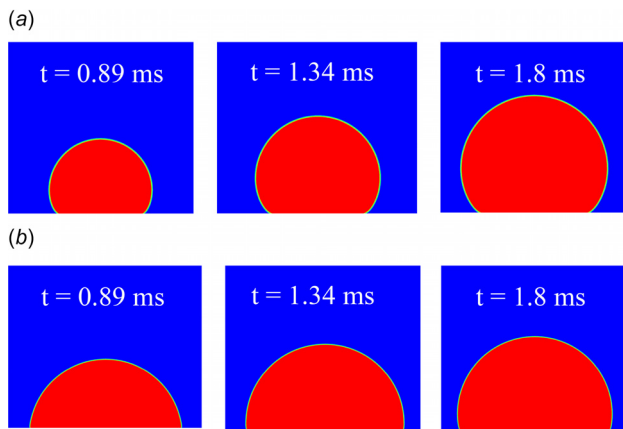

Fig. 11 The effect of width of the hydrophilic region on growth of contact angle as a function of time: (*a*) $w = 4$ μm and (*b*) $w = 12$ μm
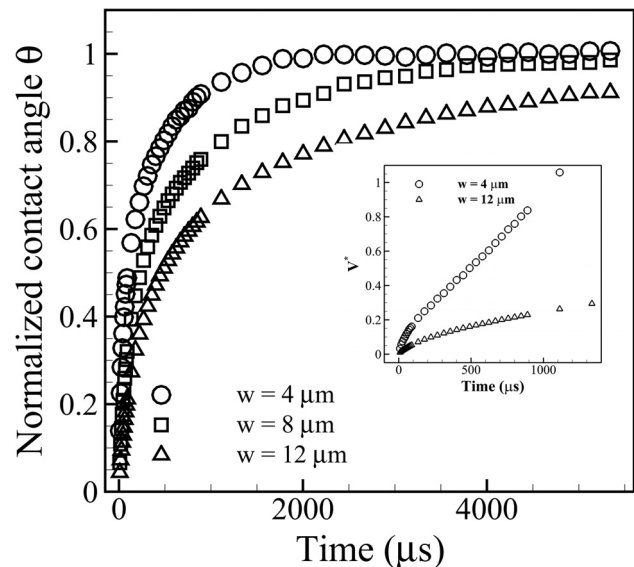

Fig. 12 The effect of width of the hydrophilic region on growth of normalized contact angle as a function of time. The normalized contact angle for droplet on the surface with hydrophilic width of $w = 4$ μm is greater than the other two surfaces. The inset plot shows the variation of normalized volume V^* of the droplet with time.

$w = 12$ μm. The contours of droplet growth with time, shown in Figs. 11(*a*) and 11(*b*), suggest that the droplet quickly reaches the hydrophobic contact angle when the hydrophilic region is small. At any instant of time in Fig. 11, the contact angle for droplet condensing on the surface with hydrophilic width $w = 4$ μm surface is greater than the contact angle of droplet condensing on the surface with hydrophilic width $w = 12$ μm. Moreover, the droplet remains pinned to the hydrophilic region for the surface with hydrophilic width $w = 12$ μm, whereas, the droplet condensing on the surface with hydrophilic width $w = 4$ μm has depinned from the hydrophilic region and has taken a nonwetting droplet shape.

In CCL growth mode, the initial contact angle of the droplet varies with the width of the hydrophilic region. In Fig. 12, we show normalized contact angle growth with time for different patterned surfaces. Here, the normalized contact angle is defined as the ratio of the contact angle of a droplet during condensation and the maximum contact angle of a droplet can achieve on the corresponding surface. The inset plot of Fig. 12 shows the variation of normalized volume V^* of the droplet with time. We defined normalized volume V^* as the ratio of the volume of droplet to that of the volume of liquid required to reach contact angle of the hydrophobic region for a given size of hydrophilic region. The normalized contact angle increases rapidly before reaching a constant value for a surface with $w = 4$ μm, compared to surfaces with

$w = 8$ μm and $w = 12$ μm, even though these surfaces ($w = 8$ μm and $w = 12$ μm) have lower thermal resistance. This is because the volume of liquid required to increase the contact angle of the drop to 140 deg differ significantly. For example, volume of liquid required for the drop condensed on surface with $w = 12$ μm to attain contact angle of 140 deg is nine times larger compared to drop on surface with $w = 4$ μm. This difference in volume required to volume of liquid condensed can be observed from the inset plot of Fig. 12.

5 Conclusions

We investigated microdroplet growth dynamics on homogeneous and patterned surfaces using two-dimensional thermal lattice Boltzmann method. The results on homogeneous surface showed that droplet follows the growth power law $R \sim t^\mu$, where power law exponent is $\mu = 1/2$. The droplet grows at higher rate on a

surface with higher wettability which is attributed to low conduction resistance and high solid–liquid contact area. We also performed simulations on patterned surfaces and observed that droplet preferentially nucleates on hydrophilic region and spreads rapidly in lateral direction forming a wet spot. Due to the effect of contact line pinning at the interface of hydrophilic–hydrophobic region, the droplet is found to grow in CCL mode with increase in contact angle. As the contact angle reaches the maximum value of hydrophobic surface, contact line depins and droplet shows CCA growth mode. We also discussed the effect of characteristic width of hydrophilic region on growth of droplet. We observed that the smaller hydrophilic region allows the droplet to achieve nonwetting shape faster than the large hydrophilic regions. On a surface with lower width of hydrophilic region, the contact angle of the droplet increases rapidly and reaches the contact angle of the hydrophobic region.

Nomenclature

a, b = parameters in the P–R equation of state
c = lattice constant
c_s = speed of sound
c_v = specific heat at constant volume
$\mathbf{F}$ = force
G = interaction parameter between fluid–fluid interactions
G_{ads} = interaction parameter between fluid–solid interactions
h_{fg} = latent heat of vaporization
Ja = Jacob number
p = pressure
R = gas constant
R, d, h = droplet radius, base diameter, and height, respectively
T = temperature
$\mathbf{u}$ = velocity
V = volume
w = width of hydrophilic region

Greek Symbols

α = thermal diffusivity
θ = contact angle
λ = thermal conductivity
μ = power law exponent
ν = kinematic viscosity
ρ = density
σ = surface tension coefficient
τ = nondimensional relaxation time
ϵ = parameter in the P–R equation of state
ϕ = source term
ψ = pseudo-potential

Subscripts

ads = adhesive force
cr = critical values
int = interaction force
interface = position of the liquid-vapor interface
l = liquid
lu = lattice units
p = physical units
s = saturation
v = vapor
w = surface or wall

References

[1] Beér, J. M., 2007, "High Efficiency Electric Power Generation: The Environmental Role," Prog. Energy Combust. Sci., **33**(2), pp. 107–134.
[2] Lee, A., Moon, M.-W., Lim, H., Kim, W.-D., and Kim, H.-Y., 2012, "Water Harvest Via Dewing," Langmuir, **28**(27), pp. 10183–10191.
[3] Khawaji, A. D., Kutubkhanah, I. K., and Wie, J.-M., 2008, "Advances in Seawater Desalination Technologies," Desalination, **221**(1–3), pp. 47–69.
[4] Kim, M., and Corradini, M., 1990, "Modeling of Condensation Heat Transfer in a Reactor Containment," Nucl. Eng. Des., **118**(2), pp. 193–212.
[5] Singh, M., Kondaraju, S., and Bahga, S. S., 2017, "Enhancement of Thermal Performance of Micro Heat Pipes Using Wettability Gradients," Int. J. Heat Mass Transfer, **104**, pp. 400–408.
[6] Carey, V. P., 2007, *Liquid–Vapor Phase-Change Phenomena: An Introduction to the Thermophysics of Vaporization and Condensation Process in Heat Transfer Equipment*, Taylor & Francis, New York.
[7] Graham, C., and Griffith, P., 1973, "Drop Size Distributions and Heat Transfer in Dropwise Condensation," Int. J. Heat Mass Transfer, **16**(2), pp. 337–346.
[8] Leach, R., Stevens, F., Langford, S., and Dickinson, J., 2006, "Dropwise Condensation: Experiments and Simulations of Nucleation and Growth of Water Drops in a Cooling System," Langmuir, **22**(21), pp. 8864–8872.
[9] Rykaczewski, K., 2012, "Microdroplet Growth Mechanism During Water Condensation on Superhydrophobic Surfaces," Langmuir, **28**(20), pp. 7720–7729.
[10] Varanasi, K. K., Hsu, M., Bhate, N., Yang, W., and Deng, T., 2009, "Spatial Control in the Heterogeneous Nucleation of Water," Appl. Phys. Lett., **95**(9), p. 094101.
[11] Hou, Y., Yu, M., Chen, X., Wang, Z., and Yao, S., 2015, "Recurrent Filmwise and Dropwise Condensation on a Beetle Mimetic Surface," ACS Nano, **9**(1), pp. 71–81.
[12] Da Riva, E., and Del Col, D., 2012, "Numerical Simulation of Laminar Liquid Film Condensation in a Horizontal Circular Minichannel," ASME J. Heat Transfer, **134**(5), p. 051019.
[13] Ganapathy, H., Shooshtari, A., Choo, K., Dessiatoun, S., Alshehhi, M., and Ohadi, M., 2013, "Volume of Fluid-Based Numerical Modeling of Condensation Heat Transfer and Fluid Flow Characteristics in Microchannels," Int. J. Heat Mass Transfer, **65**, pp. 62–72.
[14] Chen, S., Yang, Z., Duan, Y., Chen, Y., and Wu, D., 2014, "Simulation of Condensation Flow in a Rectangular Microchannel," Chem. Eng. Process.: Process Intensif., **76**, pp. 60–69.
[15] Son, G., 2010, "A Level-Set Method for Analysis of Microdroplet Evaporation on a Heated Surface," J. Mech. Sci. Technol., **24**(4), pp. 991–997.
[16] Budaraju, A., Phirani, J., Kondaraju, S., and Bahga, S. S., 2016, "Capillary Displacement of Viscous Liquids in Geometries With Axial Variations," Langmuir, **32**(41), pp. 10513–10521.
[17] Yagub, A., Farhat, H., Kondaraju, S., and Singh, T., 2015, "A Lattice Boltzmann Model for Substrates With Regularly Structured Surface Roughness," J. Comput. Phys., **301**, pp. 402–414.
[18] Farhat, H., Kondaraju, S., Na, S.-K., and Lee, J. S., 2013, "Effect of Hydrodynamic and Fluid-Solid Interaction Forces on the Shape and Stability of a Droplet Sedimenting on a Horizontal Wall," Phys. Rev. E, **88**, p. 013013.
[19] Li, Q., Luo, K., Kang, Q., He, Y., Chen, Q., and Liu, Q., 2016, "Lattice Boltzmann Methods for Multiphase Flow and Phase-Change Heat Transfer," Prog. Energy Combust. Sci., **52**, pp. 62–105.
[20] Shan, X., and Chen, H., 1993, "Lattice Boltzmann Model for Simulating Flows With Multiple Phases and Components," Phys. Rev. E, **47**(3), pp. 1815–1819.
[21] Shan, X., and Chen, H., 1994, "Simulation of Nonideal Gases and Liquid-Gas Phase Transitions by the Lattice Boltzmann Equation," Phys. Rev. E, **49**(4), pp. 2941–2948.
[22] Yuan, P., and Schaefer, L., 2006, "Equations of State in a Lattice Boltzmann Model," Phys. Fluids (1994-Present), **18**(4), p. 042101.
[23] Gong, S., and Cheng, P., 2012, "A Lattice Boltzmann Method for Simulation of Liquid-Vapor Phase-Change Heat Transfer," Int. J. Heat Mass Transfer, **55**(17–18), pp. 4923–4927.
[24] Liu, X., and Cheng, P., 2013, "Lattice Boltzmann Simulation of Steady Laminar Film Condensation on a Vertical Hydrophilic Subcooled Flat Plate," Int. J. Heat Mass Transfer, **62**, pp. 507–514.
[25] Liu, X., and Cheng, P., 2013, "Lattice Boltzmann Simulation for Dropwise Condensation of Vapor Along Vertical Hydrophobic Flat Plates," Int. J. Heat Mass Transfer, **64**, pp. 1041–1052.
[26] Ashrafi, A., and Moosavi, A., 2016, "Droplet Condensation on Chemically Homogeneous and Heterogeneous Surfaces," J. Appl. Phys., **120**(12), p. 124901.
[27] Li, Q., Kang, Q., Francois, M., He, Y., and Luo, K., 2015, "Lattice Boltzmann Modeling of Boiling Heat Transfer: The Boiling Curve and the Effects of Wettability," Int. J. Heat Mass Transfer, **85**, pp. 787–796.
[28] Bhatnagar, P. L., Gross, E. P., and Krook, M., 1954, "A Model for Collision Processes in Gases. I. small Amplitude Processes in Charged and Neutral One-Component Systems," Phys. Rev., **94**(3), pp. 511–525.
[29] Qian, Y. H., D'Humières, D., and Lallemand, P., 1992, "Lattice BGK Models for Navier–Stokes Equation," EPL (Europhys. Lett.), **17**(6), p. 479.

[30] Kupershtokh, A., Medvedev, D., and Karpov, D., 2009, "On Equations of State in a Lattice Boltzmann Method," Comput. Math. Appl., **58**(5), pp. 965–974.

[31] Jain, P. K., Tentner, A., and Uddin, R., 2009, "A Lattice Boltzmann Framework to Simulate Boiling Water Reactor Core Hydrodynamics," Comput. Math. Appl., **58**(5), pp. 975–986.

[32] Sukope, M. C., and Thorne, D. T., 2006, *Lattice Boltzmann Modeling: An Introduction for Geoscientists and Engineers*, Springer-Verlag, Berlin.

[33] Angelopoulos, A. D., Paunov, V. N., Burganos, V. N., and Payatakes, A. C., 1998, "Lattice Boltzmann Simulation of Nonideal Vapor-Liquid Flow in Porous Media," Phys. Rev. E, **57**(3), pp. 3237–3245.

[34] Briant, A. J., Wagner, A. J., and Yeomans, J. M., 2004, "Lattice Boltzmann Simulations of Contact Line Motion—I: Liquid-Gas Systems," Phys. Rev. E, **69**(3 Pt. 1), p. 031602.

[35] Mohamad, A. A., 2011, *Lattice Boltzmann Method: Fundamentals and Engineering Applications With Computer Codes*, Springer-Verlag, London.

[36] Narhe, R. D., and Beysens, D. A., 2004, "Nucleation and Growth on a Superhydrophobic Grooved Surface," Phys. Rev. Lett., **93**(7), p. 076103.

[37] Narhe, R. D., and Beysens, D. A., 2007, "Growth Dynamics of Water Drops on a Square-Pattern Rough Hydrophobic Surface," Langmuir, **23**(12), pp. 6486–6489.

[38] Beysens, D., 2006, "Dew Nucleation and Growth," C. R. Phys., **7**(9–10), pp. 1082–1100.

[39] Kelton, K., and Greer, A., 2010, *Nucleation in Condensed Matter: Applications in Materials and Biology*, Elsevier, Oxford, UK.

[40] Xu, W., Lan, Z., Peng, B. L., Wen, R. F., and Ma, X. H., 2015, "Effect of Surface Free Energies on the Heterogeneous Nucleation of Water Droplet: A Molecular Dynamics Simulation Approach," J. Chem. Phys., **142**(5), p. 054701.